Slowly rotating superfluid neutron stars with isospin dependent entrainment in a two-fluid model

Apurba Kheto and Debades Bandyopadhyay

Astroparticle Physics and Cosmology Division and Centre for Astroparticle Physics,
Saha Institute of Nuclear Physics, 1/AF Bidhannagar, Kolkata 700064, India

We investigate the slowly rotating general relativistic superfluid neutron stars including the entrainment effect in a two-fluid model, where one fluid represents the superfluid neutrons and the other is the charge-neutral fluid, called the proton fluid, made of protons and electrons. The equation of state and the entrainment effect between the superfluid neutrons and the proton fluid are computed using a relativistic mean field (RMF) model where baryon-baryon interaction is mediated by the exchange of σ, ω, and ρ mesons, and scalar self-interactions are also included. The equations governing rotating neutron stars in the slow rotation approximation are second order in rotational velocities of neutron and proton fluids. We explore the effects of the isospin dependent entrainment and the relative rotation between two fluids on the global properties of rotating superfluid neutron stars such as mass, shape, and the mass-shedding (Kepler) limit within the RMF model with different parameter sets. It is observed that for the global properties of rotating superfluid neutron stars in particular, the Kepler limit is modified compared with the case that does not include the contribution of ρ mesons in the entrainment effect.

I. INTRODUCTION

The study of superfluid dynamics in neutron stars has gained momentum recently with the observation of fast cooling of the neutron star in Cassiopeia A (Cas A) [1]. It has been inferred that the rapid cooling in the neutron star in Cas A might be the outcome of neutron superfluidity in its interior [2]. The glitch phenomenon in neutron stars might also be strong evidence of the superfluidity in the crust and core of a neutron star [3–6]. There might be an interplay between the superfluidity in neutron stars and superfluidity studied in the laboratory. One important aspect of the superfluidity is the entrainment effect, which was found in a mixture of superfluid ^{3}He and ^{4}He in the laboratory [7]. A similar effect might occur in superfluid neutron stars when neutron and proton fluids pass through each other. In this case, the two fluids are coupled because the momentum of one fluid carries along with it some mass current of the other fluid. This is known as the entrainment effect.

The entrainment effect in superfluid neutron star matter was calculated in relativistic mean field (RMF) models [8,9]. Comer and Joynt exploited the σ-ω Walecka model for this purpose. However, neutron star matter is highly asymmetric, and the role of symmetry energy is very important in determining the equation of state (EOS) and the structures of neutron stars. It is expected that the symmetry energy might also influence the entrainment effect. Recently we investigated the entrainment effect in the RMF model including ρ mesons [9]. We showed that the symmetry energy significantly affected the entrainment effect compared to the case without ρ mesons [9]. It may be

worth mentioning here that the dependence of the entrainment effect on the symmetry energy was also studied using polytropic equations of state [10,11] as well as with relativistic Fermi liquid theory [12–15].

The role of the entrainment effect in rotating neutron stars was investigated in Newtonian as well as general relativistic formulations by different groups [10,11,16]. In some of those calculations, the dependence of the entrainment effect on the symmetry energy was considered through the polytropic EOS [10,11]. However, so far, there is no calculation of rotating neutron stars based on the isospin dependent entrainment effect derived from a realistic EOS.

In this paper, we are interested in the role of isospin dependent entrainment on slowly rotating superfluid neutron stars. Here we adopt the two-fluid formalism for slowly rotating superfluid neutron stars as described in Ref. [17]. The paper is organized in the following way. In Sec. II we describe the formalism for calculating the isospin dependent entrainment in a RMF model of dense baryonic matter, and the application of Hartle's slow rotation approximation to Einstein's field equations for superfluid neutron stars. We discuss results in Sec. III. Section IV gives the summary and conclusion.

II. METHODOLOGY

A. The superfluid formalism

Here we consider the superfluid formalism developed by various groups [17–23]. The signature of the metric used here is the same as in Ref. [8]. The master function (Λ) in the superfluid formalism is a function of three scalars,

$n^2 = -n_\mu n^\mu$, $p^2 = -p_\mu p^\mu$, and $x^2 = -n_\mu p^\mu$, which are constructed from neutron (n^μ) and proton (p^μ) number density currents. It may be noted that $-\Lambda(n^2, p^2, x^2)$ corresponds to the total thermodynamic energy density when neutron and proton fluids are comoving. The stress-energy tensor is written as [8,16]

$$T_\nu^\mu = \Psi \delta_\nu^\mu + n^\mu \mu_\nu + p^\mu \chi_\nu \qquad (1)$$

and the generalized pressure is given by

$$\Psi = \Lambda - n^\rho \mu_\rho - p^\rho \chi_\rho. \qquad (2)$$

The neutron and proton momentum covectors

$$\mu_\nu = \mathcal{B} n_\nu + \mathcal{A} p_\nu, \qquad (3)$$

$$\chi_\nu = \mathcal{A} n_\nu + \mathcal{C} p_\nu, \qquad (4)$$

are conjugate to n^μ and p^μ, respectively. It is manifestly evident that neutron or proton momentum is a linear combination of both number density currents, the magnitudes of which are chemical potentials of neutron and proton fluids, respectively [8]. The charge-neutral proton fluid is composed of protons and electrons, and it was shown that the chemical potential of the proton fluid is the sum of proton and electron chemical potentials [24,25]. The master function is independent of the entrainment

effect; i.e., $x^2 = 0$ when the coefficient $\mathcal{A}$ is zero. One obtains the coefficients of Eqs. (3) and (4) from the master function,

$$\mathcal{A} = -\frac{\partial \Lambda}{\partial x^2}, \qquad \mathcal{B} = -2\frac{\partial \Lambda}{\partial n^2}, \qquad \mathcal{C} = -2\frac{\partial \Lambda}{\partial p^2}. \qquad (5)$$

The field equations for neutrons and protons involve two conservation equations as well as two Euler equations.

In the slow rotation approximation, the master function is written in terms of $x^2 - np$, which is small with respect to np [8],

$$\Lambda(n^2, p^2, x^2) = \sum_{i=0}^{\infty} \gamma_i(n^2, p^2)(x^2 - np)^i. \qquad (6)$$

Using this form of master function, the coefficients $\mathcal{A}$, $\mathcal{A}_0^0$, etc., that determine the nonrotating background configuration are calculated easily [8,16].

For the slow rotation approximation, we are interested in terms up to second order in the rotational velocities of neutrons and protons. This corresponds to the terms proportional to $x^2 - np$ in the master function. It may be noted that the following combinations appearing in the field equations are dependent on γ_1 when computed on the background [16]:

$$A + n\frac{\partial A}{\partial n} + np\frac{\partial A}{\partial x^2} = -\gamma_1 - n\frac{\partial \gamma_1}{\partial n} - \sum_{i=2}^{\infty} \left(\gamma_i + n\frac{\partial \gamma_i}{\partial n}\right)(x^2 - np)^{i-1}, \qquad (7)$$

$$A + p\frac{\partial A}{\partial p} + np\frac{\partial A}{\partial x^2} = -\gamma_1 - p\frac{\partial \gamma_1}{\partial p} - \sum_{i=2}^{\infty} \left(\gamma_i + p\frac{\partial \gamma_i}{\partial p}\right)(x^2 - np)^{i-1}. \qquad (8)$$

The calculation of the master function in the RMF model was described in detail in Refs. [8,9]. Unlike the calculation of Comer and Joynt [8], the role of symmetry energy on the master function and the entrainment effect was considered in Ref. [9]. In the latter case, the relativistic σ-ω-ρ model, including scalar meson self-interactions [26], was used to derive the master function [9]. The Lagrangian density for nucleon-nucleon interaction has the form [27]

$$\begin{aligned}
\mathcal{L}_B = &\sum_{B=n,p} \bar{\Psi}_B(i\gamma_\mu \partial^\mu - m_B + g_{\sigma B}\sigma - g_{\omega B}\gamma_\mu \omega^\mu - g_{\rho B}\gamma_\mu \mathbf{t}_B \cdot \boldsymbol{\rho}^\mu)\Psi_B \\
&+ \frac{1}{2}(\partial_\mu \sigma \partial^\mu \sigma - m_\sigma^2 \sigma^2) - \frac{1}{3}bm(g_\sigma \sigma)^3 - \frac{1}{4}c(g_\sigma \sigma)^4 \\
&- \frac{1}{4}\omega_{\mu\nu}\omega^{\mu\nu} + \frac{1}{2}m_\omega^2 \omega_\mu \omega^\mu - \frac{1}{4}\boldsymbol{\rho}_{\mu\nu} \cdot \boldsymbol{\rho}^{\mu\nu} + \frac{1}{2}m_\rho^2 \boldsymbol{\rho}_\mu \cdot \boldsymbol{\rho}^\mu.
\end{aligned} \qquad (9)$$

The Dirac nucleon effective mass m_* is defined as $m_* = m - \langle g_\sigma \sigma \rangle$ where the nucleon mass (m) is taken as the average of bare neutron (m_n) and proton (m_p) masses. The frame in which neutrons have zero spatial momentum and protons have a wave vector $k_\mu = (k_0, 0, 0, K)$ [8] is chosen to solve the equations of motion for meson fields in the mean field approximation [27].

The master function, generalized pressure, and chemical potentials of neutron and proton fluids in the limit $K \to 0$ are given by

$$\Lambda|_0 = -\frac{c_\omega^2}{18\pi^4}(k_n^3 + k_p^3)^2 - \frac{c_\rho^2}{72\pi^4}(k_p^3 - k_n^3)^2 - \frac{1}{4\pi^2}\left(k_n^3\sqrt{k_n^2 + m_*^2|_0} + k_p^3\sqrt{k_p^2 + m_*^2|_0}\right)$$
$$-\frac{1}{4}c_\sigma^{-2}[(2m - m_*|_0)(m - m_*|_0) + m_*|_0(bmc_\sigma^2(m - m_*|_0)^2 + cc_\sigma^2(m - m_*|_0)^3)]$$
$$-\frac{1}{3}bm(m - m_*|_0)^3 - \frac{1}{4}c(m - m_*|_0)^4 - \frac{1}{8\pi^2}\left(k_p[2k_p^2 + m_e^2]\sqrt{k_p^2 + m_e^2} - m_e^4\ln\left[\frac{k_p + \sqrt{k_p^2 + m_e^2}}{m_e}\right]\right), \quad (10)$$

$$\mu|_0 = -\frac{\pi^2}{k_n^2}\frac{\partial\Lambda}{\partial k_n}\bigg|_0 = \frac{c_\omega^2}{3\pi^2}(k_n^3 + k_p^3) - \frac{c_\rho^2}{12\pi^2}(k_p^3 - k_n^3) + \sqrt{k_n^2 + m_*^2|_0}, \quad (11)$$

$$\chi|_0 = -\frac{\pi^2}{k_p^2}\frac{\partial\Lambda}{\partial k_p}\bigg|_0 = \frac{c_\omega^2}{3\pi^2}(k_n^3 + k_p^3) + \frac{c_\rho^2}{12\pi^2}(k_p^3 - k_n^3) + \sqrt{k_p^2 + m_*^2|_0} + \sqrt{k_p^2 + m_e^2}, \quad (12)$$

$$\Psi|_0 = \Lambda|_0 + \frac{1}{3\pi^2}(\mu|_0 k_n^3 + \chi|_0 k_p^3), \quad (13)$$

where the subscript 0 stands for quantities calculated in the limit $K \to 0$, $c_\sigma^2 = (g_\sigma/m_\sigma)^2$, $c_\omega^2 = (g_\omega/m_\omega)^2$, and $c_\rho^2 = (g_\rho/m_\rho)^2$, and

$$m_*|_0 = m_*(k_n, k_p, 0)$$
$$= m - m_*|_0\frac{c_\sigma^2}{2\pi^2}\left(k_n\sqrt{k_n^2 + m_*^2|_0} + k_p\sqrt{k_p^2 + m_*^2|_0} + \frac{1}{2}m_*^2|_0\ln\left[\frac{-k_n + \sqrt{k_n^2 + m_*^2|_0}}{k_n + \sqrt{k_n^2 + m_*^2|_0}}\right]\right.$$
$$\left. + \frac{1}{2}m_*^2|_0\ln\left[\frac{-k_p + \sqrt{k_p^2 + m_*^2|_0}}{k_p + \sqrt{k_p^2 + m_*^2|_0}}\right]\right) + bmc_\sigma^2(m - m_*)^2 + cc_\sigma^2(m - m_*)^3. \quad (14)$$

It is to be noted here that electrons are treated as non-interacting relativistic particles and are included in the calculation of the master function and generalized pressure. The values of the various coefficients $\mathcal{A}|_0$, $\mathcal{B}|_0$, $\mathcal{C}|_0$, $\mathcal{A}_0^0|_0$, $\mathcal{B}_0^0|_0$, and $\mathcal{C}_0^0|_0$ that appear in the field equations are provided in the Appendix.

B. Slowly rotating superfluid neutron stars

Andersson and Comer [17] extended Hartle's slow rotation formalism for the single fluid [28] to the case of the two-fluid model in order to describe superfluid neutron stars. They considered that the superfluid neutron and the proton fluid are rotating with different rotational velocities. However, they did not include the entrainment effect in their calculation. Here we adopt the two-fluid formalism of Andersson and Comer as described by Refs. [16,17] to study stationary, axisymmetric, and asymptotically flat configurations. Furthermore, we introduce the isospin dependent entrainment in this calculation. In the slow rotation approximation, rotational velocities of neutron (Ω_n) and proton (Ω_p) fluids are considered as small so that inequalities $\Omega_n R \ll c$ and $\Omega_p R \ll c$ are satisfied, where c is the speed of light. The slow rotation acts as

the perturbation on nonrotating configurations. We retain terms up to second order in the angular velocities of neutron and proton fluids in field equations in the slow rotation approximation. The metric used here has the following structure [16,17,28]:

$$g_{\mu\nu}dx^\mu dx^\nu = -(N^2 - \sin^2\theta K[N^\phi]^2)dt^2 + Vd\tilde{r}^2$$
$$- 2KN^\phi\sin^2\theta dt d\phi + K(d\theta^2 + \sin^2\theta d\phi^2). \quad (15)$$

The equations relevant for the metric variables in the two-fluid model and the slow rotation approximation are same as those of Hartle's single-fluid model, and the metric functions are expanded in powers of angular velocities [16,17,28],

$$N = e^{\nu(\tilde{r})/2}(1 + h(\tilde{r}, \theta)),$$
$$V = e^{\lambda(\tilde{r})}(1 + 2v(\tilde{r}, \theta)),$$
$$K = \tilde{r}^2(1 + 2k(\tilde{r}, \theta)),$$
$$N^\phi = \omega(\tilde{r}), \quad (16)$$

where ω is a first-order quantity in the angular velocities, and h, v, and k are second-order quantities. Further, h, v, and k are decomposed into $\ell = 0$ and $\ell = 2$ terms after expanding those in spherical harmonics,

$$h = h_0(\tilde{r}) + h_2(\tilde{r})P_2(\cos\theta),$$
$$v = v_0(\tilde{r}) + v_2(\tilde{r})P_2(\cos\theta),$$
$$k = k_2(\tilde{r})P_2(\cos\theta), \tag{17}$$

where $P_2(\cos\theta) = (3\cos^2\theta - 1)/2$.

Similarly, neutron (n) and proton (p) number densities are expanded as

$$n = n_0(\tilde{r})(1 + \eta(\tilde{r},\theta)), \qquad p = p_0(\tilde{r})(1 + \Phi(\tilde{r},\theta)), \tag{18}$$

where terms η and Φ are of $\mathcal{O}(\Omega_{n,p}^2)$,

$$\eta = \eta_0(\tilde{r}) + \eta_2(\tilde{r})P_2(\cos\theta),$$
$$\Phi = \Phi_0(\tilde{r}) + \Phi_2(\tilde{r})P_2(\cos\theta). \tag{19}$$

A coordinate transformation $\tilde{r} \to r + \xi(r,\theta)$ is introduced such that $\Lambda(\tilde{r}(r,\theta),\theta) = \Lambda_0(r)$ [17]. Here the ξ coordinate is also expanded in spherical harmonics as $\xi = \xi_0(r) + \xi_2(r)P_2(\cos\theta)$.

With this prescription of the slow rotation approximation for metric functions, as well as neutron and proton densities along with the coordinate transformation, the fluid and Einstein field equations are reduced to four sets of equations. The first set of equations corresponds to nonrotating background configurations that are obtained from the solutions of two background metric components, λ and ν [16,17]. Those are given in terms of coefficients of fluid equations,

$$A_0^0|_0 p_0' + B_0^0|_0 n_0' + \frac{1}{2}\mu|_0\nu' = 0,$$
$$C_0^0|_0 p_0' + A_0^0|_0 n_0' + \frac{1}{2}\chi|_0\nu' = 0, \tag{20}$$

where prime denotes differentiation with respect to $\tilde{r}$, and $A_0^0|_0$, $B_0^0|_0$, and $C_0^0|_0$ coefficients are obtained from the master function and are taken from Ref. [9]. The regularity condition demands that λ, λ', ν', n_0', and p_0' vanish at the origin. The total mass of this configuration is

$$M = -4\pi \int_0^R \Lambda_0(\tilde{r})\tilde{r}^2 d\tilde{r}. \tag{21}$$

Next, the frame dragging $\omega(r)$, which is first order in angular velocities of neutron and proton fluids, is obtained from the following equation [16,28]:

$$\frac{1}{r^4}\frac{d}{dr}\left(r^4 e^{-(\lambda+\nu)/2}\frac{d\tilde{L}_n}{dr}\right) - 16\pi e^{(\lambda-\nu)/2}(\Psi_0 - \Lambda_0)\tilde{L}_n$$
$$= 16\pi e^{(\lambda-\nu)/2}\chi_0 p_0(\Omega_n - \Omega_p). \tag{22}$$

This equation has the same structure as that of the single fluid except for the nonzero term on the right-hand side [28]. Here we define $\tilde{L}_n = \omega - \Omega_n$ and $\tilde{L}_p = \omega - \Omega_p$, which represent the rotational frequencies as measured by a distant observer. The boundary condition implies that the interior solution of $\omega(r)$ matches with the vacuum solution

$$\tilde{L}_n(R) = -\Omega_n + \frac{2J}{R^3}, \tag{23}$$

where J is the total angular momentum of the system. The derivative of the solution is also continuous at the surface [16].

The neutron and proton angular momenta, J_n and J_p, respectively, are given by [17]

$$J_n = -\frac{8\pi}{3}\int_0^R dr r^4 e^{(\lambda-\nu)/2}[\mu_0 n_0\tilde{L}_n + A_0 n_0 p_0(\Omega_n - \Omega_p)] \tag{24}$$

and

$$J_p = -\frac{8\pi}{3}\int_0^R dr r^4 e^{(\lambda-\nu)/2}[\chi_0 p_0\tilde{L}_p + A_0 n_0 p_0(\Omega_p - \Omega_n)]. \tag{25}$$

The total angular momentum J is equal to $J_n + J_p$.

The last two sets of equations are $\mathcal{O}(\Omega_{n,p}^2)$ equations. One can obtain ξ_0, η_0, Φ_0, h_0, and v_0 from $\ell = 0$ second-order equations; on the other hand, ξ_2, η_2, Φ_2, h_2, v_2, and k_2 follow from $\ell = 2$ second-order equations. A detailed discussion of $\ell = 0$ and $\ell = 2$ second-order equations and numerical techniques to solve those equations can be found in Refs. [16,17,28]. After obtaining a complete solution in the slow rotation approximation, one can calculate the quadruple moment of the configuration and the rotationally induced change of mass as described in Refs. [16,17]. Furthermore, the Kepler frequency of the slowly rotating superfluid neutron star is obtained following the prescription of Andersson and Comer [17],

$$\Omega_K = \sqrt{\frac{M}{R^3}} - \frac{\hat{J}\Omega_p}{R^3} + \sqrt{\frac{M}{R^3}}\left\{\frac{\delta\hat{M}}{2M} + \frac{(R+3M)(3R-2M)}{4R^4 M^2}\hat{J}^2\right.$$
$$\left. - \frac{3}{4}\frac{2\hat{\xi}_0 - \hat{\xi}_2}{R} + \alpha\hat{A}\right\}\Omega_p^2, \tag{26}$$

where scaling of $J = \hat{J}\Omega_p$, $\delta M = \delta\hat{M}\Omega_p^2$, $\xi_0 = \hat{\xi}_0\Omega_p^2$, and $\xi_2 = \hat{\xi}_2\Omega_p^2$ with Ω_p is made and

TABLE I.   Nucleon-meson coupling constants corresponding to the GL and NL3 sets are taken from Refs. [27,29]. The coupling constants are obtained by reproducing the saturation properties of symmetric nuclear matter as detailed in Ref. [9]. All the coupling constants are in fm^2, except b and c, which are dimensionless. The background nonrotating configurations as computed by Kheto and Bandyopadhyay [9] are used here. The central neutron wave number $k_n(0)$ is given by fm^{-1}. The mass (M) and radius (R) are in units of $M_\odot$ and km, respectively.

	c_σ^2	c_ω^2	c_ρ^2	b	c	$\nu(0)$	$k_n(0)$	$x_p(0)$	M	R	$\eta_0(0)$
GL	12.684	7.148	4.410	0.005610	−0.006 986	−2.387 99	2.71	0.24	2.37	11.09	0.0
NL3	15.739	10.530	5.324	0.002055	−0.002 650	−2.333 19	2.40	0.23	2.82	13.17	0.0

$$\alpha = \frac{3(R^3 - 2M^3)}{4M^3} \log\left(1 - \frac{2M}{R}\right)$$
$$+ \frac{3R^4 - 3R^3M - 2R^2M^2 - 8RM^3 + 6M^4}{2RM^2(R - 2M)}. \qquad (27)$$

It is to be noted that the expression for the Kepler frequency in Eq. (26) differs from that of Eq. (77) of Ref. [17]. This difference originates from the factor at the beginning of the third term within the second bracket and the term involving $\hat{\xi}_0$ and $\hat{\xi}_2$ in both equations. We discuss this issue further in the next section. It is worth mentioning here that the model based on the slow rotation approximation is applicable for the fastest observed pulsar as noted by others [10,17]. However, this approximation breaks down near the Kepler limit [10].

III. RESULTS AND DISCUSSION

Now we discuss the results of slowly rotating superfluid neutron stars. Nonrotating background configurations are obtained by solving Eq. (20). In this context, we exploit the RMF EOS which includes the isospin dependent entrainment effect [9]. We use GL and NL3 parameter sets in this calculation, both of which are listed in Table I. Central neutron number density is an essential input for the calculation of the background configurations. The proton number density in the background model is no longer a free parameter because the chemical equilibrium is imposed at the center of the star, i.e., $\mu|_0 = \chi|_0$ [24]. The chemical equilibrium is established when both fluids are corotating. However, the chemical equilibrium does not hold good for different rotation rates of neutron and proton fluids [10,11]. Masses and radii corresponding to two nonrotating configurations are also recorded in Table I. The chosen background configurations are just below their maximum masses [9]. Furthermore, we consider $\eta_0(0) = 0$ and, consequently, $\Phi_0(0) = 0$ in all cases.

As soon as we know the background configuration, we can calculate the frame-dragging frequency from Eq. (22). As we are dealing with the two-fluid system, the central value of $\tilde{L}_n$ and relative rotation rate Ω_n/Ω_p are needed to solve Eq. (22) [17]. A rescaled Eq. (22) with the definition of $\hat{L}_n(r) = \tilde{L}_n/\Omega_p$ is solved to determine the frame-dragging frequency for different values of Ω_p using a

fixed relative rotation rate. The boundary condition of the problem demands that the interior solution matches with the known vacuum solution given by Eq. (23). The frame-dragging frequency, $\frac{\omega(r)}{\Omega_p}$, is plotted as a function of radial distance (r/R) in Fig. 1 for three different relative rotation rates. The left panel denotes the GL parameter set and the right panel represents the NL3 set. The frame-dragging frequency decreases monotonically from the center to the surface of the star for three relative rotation rates in both panels. This feature of the frame-dragging frequency is quite similar to the standard single-fluid result [30]. Further it is noted that the frame-dragging frequency is always higher for larger values of relative rotation rate.

Now we discuss numerical solutions of different metric functions of the superfluid neutron star in the slow rotation approximation. First we solve the $\ell = 0$ equations and determine ξ_0, η_0, Φ_0, h_0, and v_0 following the procedure laid down by Andersson and Comer [17]. Metric functions h_0 and v_0 match with the vacuum solutions at the surface. The metric function $v_0(r)$ as a function of radial distance is displayed in Fig. 2 for three different relative rotation rates. The left panel shows the results of the GL set and the right panel corresponds to those of the NL3 set. It is noted that
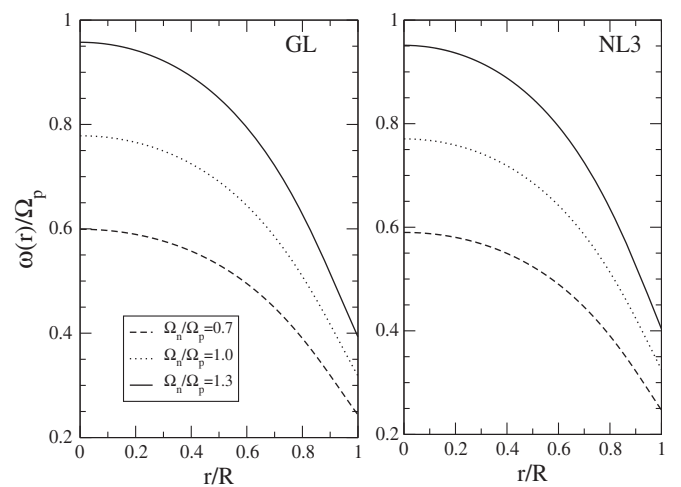

FIG. 1.   The frame-dragging frequency $\omega(r)$ is plotted as a function of radial distance (r/R) using the GL parameter set (left panel) and the NL3 parameter set (right panel) for three different relative rotation rates Ω_n/Ω_p.
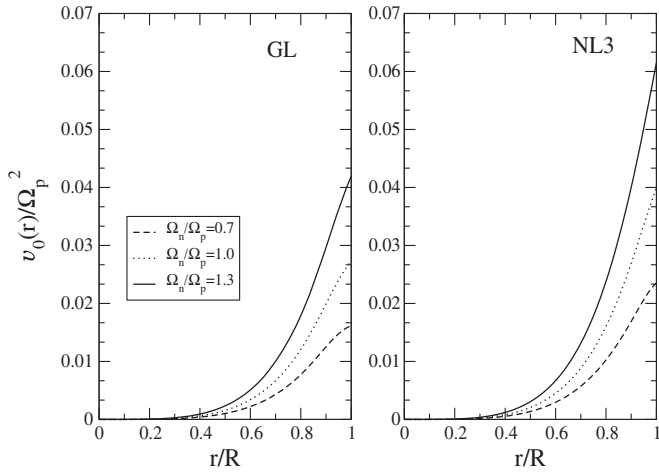
FIG. 2. The metric function $v_0(r)$ is plotted as a function of radial distance (r/R) using the GL parameter set (left panel) and the NL3 parameter set (right panel) for three different relative rotation rates Ω_n/Ω_p.

FIG. 4. The metric functions $h_0(r)$ (three lower curves) and $h_2(r)$ (three upper curves) are plotted as a function of radial distance (r/R) for three different relative rotation rates Ω_n/Ω_p. The left panel shows the results of the GL parameter set and the right panel demonstrates those of the NL3 parameter set.

the metric function v_0 increases monotonically to the surface and matches smoothly with the exterior solution. For the NL3 set, the value of this metric function at the surface is always higher than that of the GL set. A new metric function m_0 is defined in terms of v_0 and λ as $m_0 = rv_0/\exp(\lambda)$. The radial profile of m_0, which merges with the exterior solution at the surface, is shown in Fig. 3 for different relative rotation rates.

We solve the $\ell = 2$ equations in a similar way to that used for solutions of $\ell = 0$ equations [17]. A new variable, $\bar{k} = k_2 + h_2$, is introduced to solve two coupled first-order equations in h_2 and k_2 [28]. This leads to two coupled differential equations in $\bar{k}$ and h_2, which are solved using the method described by Hartle [28]. In Fig. 4, the metric functions h_0 and h_2 are plotted as a function of radial

distance for different relative rotation rates. The results of the GL and NL3 sets are shown in the left and right panels, respectively. In both panels, the lower three curves denote the metric function h_0 and the upper three curves imply the metric function h_2. Figure 5 shows the radial profiles of $\xi_0(r)$ (upper curves) and $\xi_2(r)$ (lower curves), and in Fig. 6, we have $\bar{k} = k_2 + h_2$ versus r for the GL (left panel) and NL3 (right panel) sets and three different relative rotation rates. In Fig. 5, the magnitude of $\xi_2(r)$ at the surface in the right panel is quite large with respect to that of the left panel when the relative rotation rate is larger than 1, and this function is directly related to the deformation of the star due to rotation.
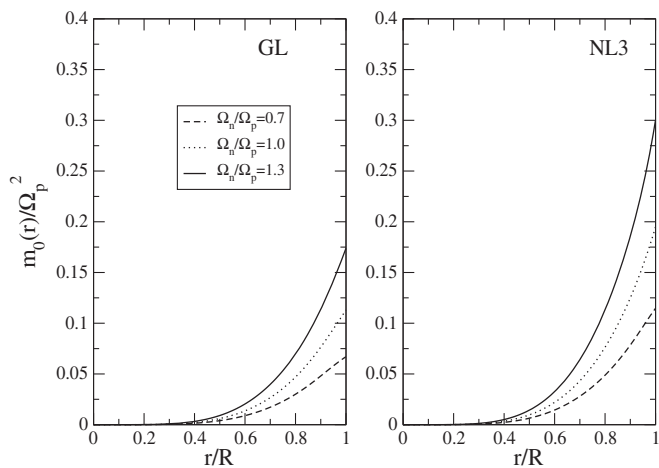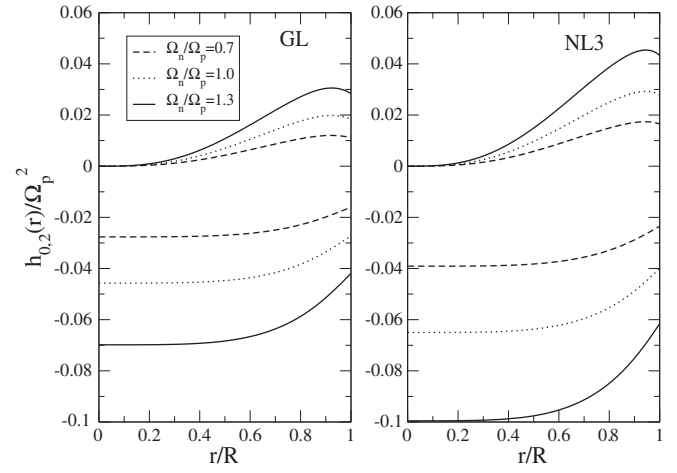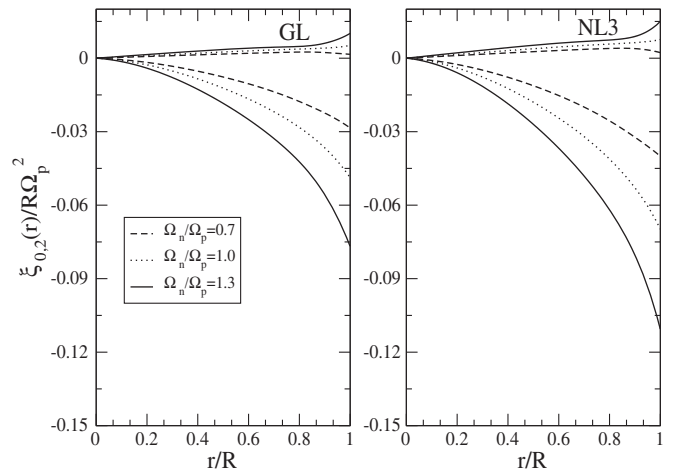

FIG. 3. The metric function $m_0(r) = rv_0(r)/\exp(\lambda(r))$ is plotted as a function of radial distance (r/R) using the GL parameter set (left panel) and the NL3 parameter set (right panel) for three different relative rotation rates Ω_n/Ω_p.

FIG. 5. The radial displacement $\xi_0(r)$ (three upper curves) and $\xi_2(r)$ (three lower curves) are plotted as a function of radial distance (r/R) for three different relative rotation rates Ω_n/Ω_p. The left panel shows the results of the GL parameter set and the right panel represents those of the NL3 parameter set.
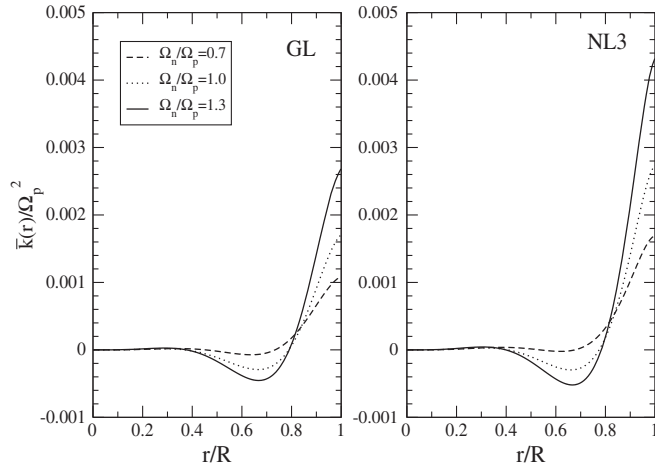
FIG. 6.   The quantity $\bar{k}$ is plotted as a function of radial distance (r/R) using the GL parameter set (left panel) and NL3 parameter set (right panel) for three different rotation rates Ω_n/Ω_p.

Figure 7 exhibits the variation of rotationally induced corrections to the neutron number density $n_0\eta_0$ (three upper curves) and $n_0\eta_2$ (three lower curves) with radius. Similarly, Fig. 8 represents the variation of rotationally induced corrections to the proton number density $p_0\Phi_0$ (three upper curves) and $p_0\Phi_2$ (three lower curves) with radius. In both cases, the left panel denotes the results of the GL set and the right panel corresponds to those of the NL3 set. We explore the role of symmetry energy on the rotationally induced corrections to the proton number density by comparing two cases with (left panel) and without (right panel) ρ mesons for the GL set in Fig. 9. For the case without ρ mesons, we consider a nonrotating configuration that is just below the maximum mass neutron star. The mass and radius of this neutron star is 2.33 $M_\odot$

FIG. 8.   The rotationally induced corrections to the proton number density $p_0(r)\phi_0(r)$ (three upper curves at $r/R = 1$) and $p_0(r)\phi_2(r)$ (three lower curves at $r/R = 1$) are plotted as a function of radial distance (r/R) using the GL parameter set (left panel) and NL3 parameter set (right panel) for three different relative rotation rates Ω_n/Ω_p.

and 10.96 km. It is noted that the corrections to the proton number density are significantly modified in the presence of ρ mesons.

The deformation of a rotating star is obtained in terms of the ratio of the polar and equatorial radii. For the slowly rotating star, this is given by $\frac{R_p}{R_e} \approx 1 + \frac{3\xi_2(R)}{2R}$. The ratio of polar to equatorial radii as a function of relative rotation rate is plotted in Fig. 10 for the GL (solid line) and NL3 (dashed line) sets. We consider the proton rotation rate to be equal to that of the fastest rotating pulsar, having spin frequency 716 Hz [31]. The nonrotating situation is
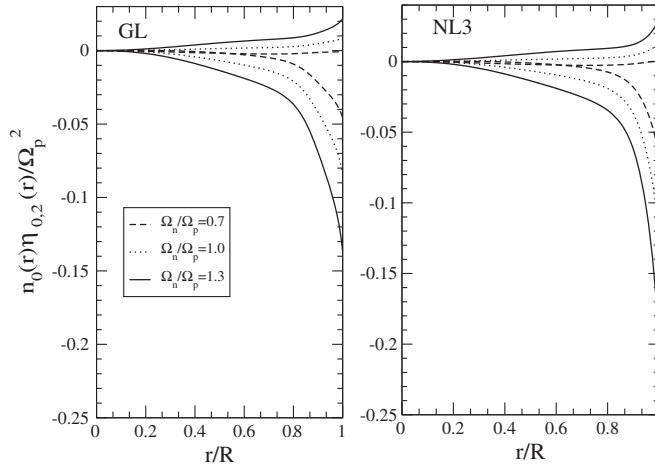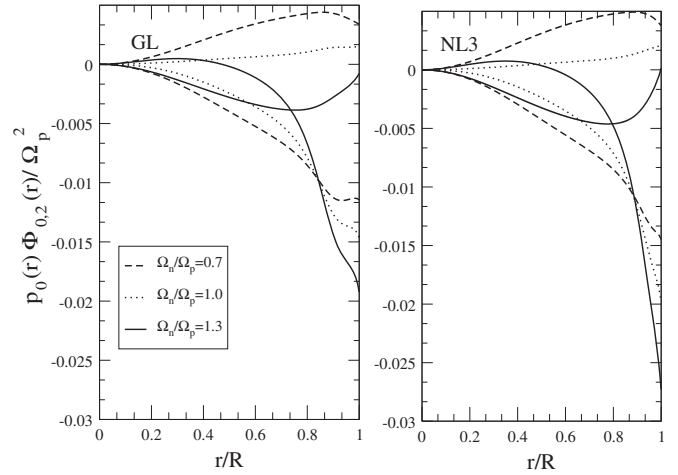

FIG. 7.   The rotationally induced corrections to the neutron number density $n_0(r)\eta_0(r)$ (three upper curves) and $n_0(r)\eta_2(r)$ (three lower curves) are plotted as a function of radial distance (r/R) for three different relative rotation rates Ω_n/Ω_p. Results of the GL and NL3 parameter sets are shown in the left and right panels, respectively.
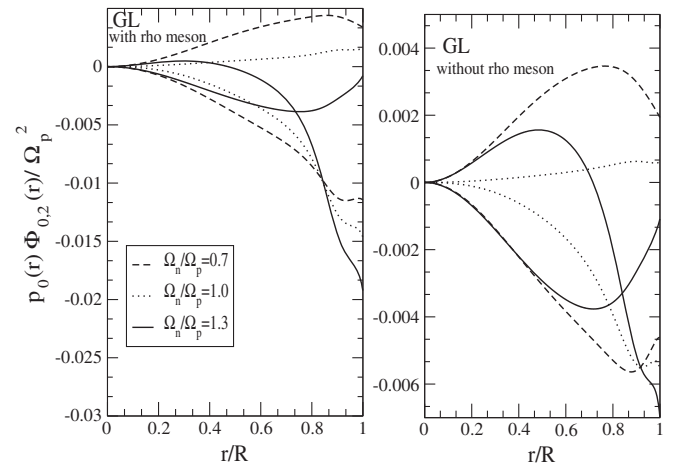

FIG. 9.   The rotationally induced corrections to the proton number density $p_0(r)\phi_0(r)$ (three upper curves at $r/R = 1$) and $p_0(r)\phi_2(r)$ (three lower curves at $r/R = 1$) are plotted as a function of radial distance (r/R) for the GL parameter set with (left panel) and without (right panel) ρ mesons for three different relative rotation rates Ω_n/Ω_p.
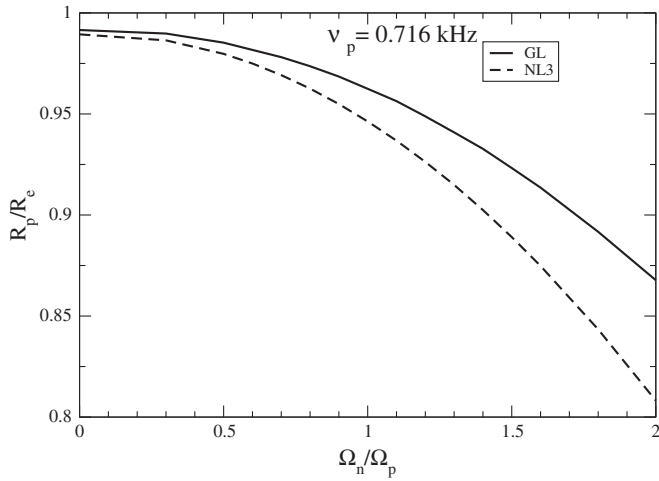
FIG. 10. The ratio of the polar to equatorial radii (R_p/R_e) is shown as a function of relative rotation rate Ω_n/Ω_p corresponding to neutron stars of masses 2.37 $M_\odot$ with the GL set (solid line) and 2.82 $M_\odot$ with the NL3 set (dashed line), respectively, considering that $\nu_p = \Omega_p/2\pi$ is equal to that of the fastest rotating pulsar, having spin frequency 716 Hz [31].

FIG. 11 (color online). The mass-shedding (Kepler) limit is shown as a function of relative rotation rate Ω_n/Ω_p for the GL set (left panel) and the NL3 set (right panel). The solid squares (green) show the allowed rotation rate of the neutron fluid (Ω_n) and the solid circles (red) show the allowed rotation rate of the proton fluid (Ω_p). The Kepler frequency is the largest of the two.

achieved when the relative rotation rate approaches zero. Furthermore we find that the rotationally induced deformation of the star is larger for the NL3 case than the GL case. This deformation increases with increasing relative rotation rate.

As neutron and proton fluids may rotate at different rates, one of them extends beyond the other at the equator. The Kepler limit is obtained from the rotation rate of the outer fluid. To determine the mass-shedding (Kepler) limit we have to solve the quadratic equation (26) for Ω_p. When $\Omega_n > \Omega_p$, the Kepler frequency is determined by the neutrons; for $\Omega_p > \Omega_n$, the Kepler frequency is determined by the protons. We calculate the Kepler limit in the RMF model including ρ mesons using the GL and NL3 parameter sets for the background configurations of Table I. The mass-shedding (Kepler) limit Ω_K as a function of relative rotation rate is plotted in Fig. 11 for the GL set (left panel) and the NL3 set (right panel). We use the radial profiles of the entrainment effect in this calculation of Kepler frequency. The results are qualitatively similar to the previous investigation by Prix and collaborators [10], though the authors in that case used some constant values of entrainment. However, our results are different from those of Comer [16]. For $\Omega_n > \Omega_p$, the Kepler frequency (solid square) approaches a constant value with increasing Ω_n. When $\Omega_n/\Omega_p < 1$, the Kepler frequency (solid circle) monotonically increases with decreasing relative rotation rate, as evident from Fig. 11, whereas the opposite scenario was found in the work of Comer [16]. On the other hand, Prix *et al.* [10] found that the Kepler limit increased monotonically as the relative rotation rate decreased. This is quite similar to our results. The difference between our results and those of Comer [16] may be due to different
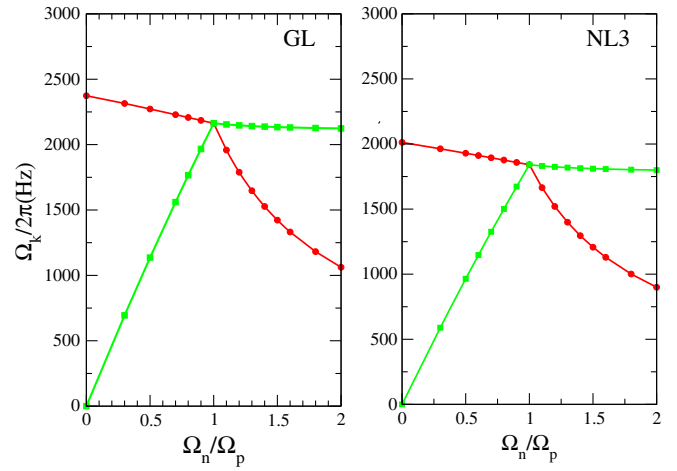
expressions for Ω_K that we have discussed in connection with Eq. (26) in Sec. II. Furthermore, Comer [16] calculated the entrainment using the equation of state obtained in the relativistic σ-ω model. Without ρ mesons, the effects of symmetry energy on the entrainment was absent. On the other hand, we exploit an isospin dependent entrainment effect calculated in the σ-ω-ρ RMF model for the determination of the Kepler limit [9]. We compare the Kepler limit calculated in the RMF model with and without ρ mesons for the GL set in Fig. 12. In both cases, we consider nonrotating configurations that are just below their
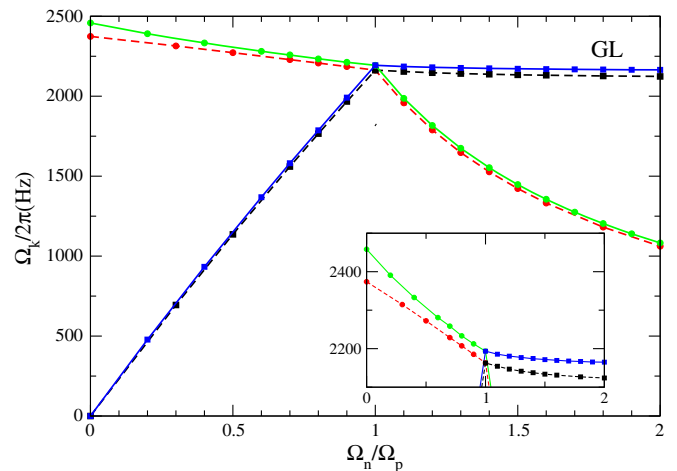

FIG. 12 (color online). The mass-shedding (Kepler) limit is shown as a function of relative rotation rate Ω_n/Ω_p with (dashed line) and without ρ mesons (solid line) for the GL set. The solid squares show the allowed rotation rate of the neutron fluid (Ω_n) and the solid circles show the allowed rotation rate of the proton fluid (Ω_p).

maximum masses, as noted in Table I and discussed in connection with Fig. 7. The solid line denotes the calculation without ρ mesons and the dashed line represents the case with ρ mesons. Furthermore, solid squares and circles correspond to allowed rotation rates of neutron and proton fluids, respectively. It is noted that the two results differ, as is evident from the highlighted part of Fig. 12.

IV. SUMMARY AND CONCLUSIONS

We have studied the role of the isospin dependent entrainment and the relative rotation rates of neutron and proton fluids on the global properties of slowly rotating superfluid neutron stars, such as the structures and the Kepler limit in the two-fluid formalism. The two-fluid formalism of Andersson and Comer [16] is adopted in our work. The effects of symmetry energy on the EOS and

entrainment are studied using the σ-ω-ρ RMF model. The symmetry energy significantly influences the rotationally induced corrections to the proton number density. It is found that the Kepler limit obtained with the isospin dependent entrainment effect is lower than that of the case when the isospin term is neglected in the entrainment effect. The behavior of the Kepler limit as a function of the relative rotation rate in our case is qualitatively similar to the results of Prix *et al.* [10] obtained using the polytropic EOS. The calculation of slowly rotating superfluid neutron stars including the isospin dependent entrainment effect in a realistic EOS is the first of its kind.

APPENDIX

The values of some useful matter coefficients (see [9]) that are the inputs of field equations are the following

$$
\begin{aligned}
\mathcal{A}|_0 &= c_\omega^2 - \frac{1}{4}c_\rho^2 + \frac{c_\omega^2}{5\mu^2|_0}\left(2k_p^2\frac{\sqrt{k_n^2+m_*^2|_0}}{\sqrt{k_p^2+m_*^2|_0}} + \frac{c_\omega^2}{3\pi^2}\left[\frac{k_n^2 k_p^3}{\sqrt{k_n^2+m_*^2|_0}} + \frac{k_p^2 k_n^3}{\sqrt{k_p^2+m_*^2|_0}}\right]\right) \\
&\quad + \frac{c_\rho^2}{20\mu^2|_0}\left(2k_p^2\frac{\sqrt{k_n^2+m_*^2|_0}}{\sqrt{k_p^2+m_*^2|_0}} + \frac{c_\rho^2}{12\pi^2}\left[\frac{k_n^2 k_p^3}{\sqrt{k_n^2+m_*^2|_0}} + \frac{k_p^2 k_n^3}{\sqrt{k_p^2+m_*^2|_0}}\right]\right) \\
&\quad - \frac{c_\rho^2 c_\omega^2}{30\mu^2|_0\pi^2}\left[\frac{k_n^2 k_p^3}{\sqrt{k_n^2+m_*^2|_0}} - \frac{k_p^2 k_n^3}{\sqrt{k_p^2+m_*^2|_0}}\right] + \frac{3\pi^2 k_p^2}{5\mu^2|_0 k_n^3}\frac{k_n^2+m_*^2|_0}{\sqrt{k_p^2+m_*^2|_0}},
\end{aligned}
\tag{A1}
$$

$$
\begin{aligned}
\mathcal{B}|_0 &= \frac{3\pi^2\mu|_0}{k_n^3} - c_\omega^2\frac{k_p^3}{k_n^3} + \frac{1}{4}c_\rho^2\frac{k_p^3}{k_n^3} - \frac{c_\omega^2 k_p^3}{5\mu^2|_0 k_n^3}\left(2k_p^2\frac{\sqrt{k_n^2+m_*^2|_0}}{\sqrt{k_p^2+m_*^2|_0}} + \frac{c_\omega^2}{3\pi^2}\left[\frac{k_n^2 k_p^3}{\sqrt{k_n^2+m_*^2|_0}} + \frac{k_p^2 k_n^3}{\sqrt{k_p^2+m_*^2|_0}}\right]\right) \\
&\quad - \frac{c_\rho^2 k_p^3}{20\mu^2|_0 k_n^3}\left(2k_p^2\frac{\sqrt{k_n^2+m_*^2|_0}}{\sqrt{k_p^2+m_*^2|_0}} + \frac{c_\rho^2}{12\pi^2}\left[\frac{k_n^2 k_p^3}{\sqrt{k_n^2+m_*^2|_0}} + \frac{k_p^2 k_n^3}{\sqrt{k_p^2+m_*^2|_0}}\right]\right) \\
&\quad + \frac{c_\rho^2 c_\omega^2 k_p^3}{30\pi^2\mu^2|_0 k_n^3}\left[\frac{k_n^2 k_p^3}{\sqrt{k_n^2+m_*^2|_0}} - \frac{k_p^2 k_n^3}{\sqrt{k_p^2+m_*^2|_0}}\right] - \frac{3\pi^2 k_p^5}{5\mu^2|_0 k_n^6}\frac{k_n^2+m_*^2|_0}{\sqrt{k_p^2+m_*^2|_0}},
\end{aligned}
\tag{A2}
$$

$$
\begin{aligned}
\mathcal{C}|_0 &= \frac{3\pi^2\chi|_0}{k_p^3} + \frac{1}{4}c_\rho^2\frac{k_n^3}{k_p^3} - c_\omega^2\frac{k_n^3}{k_p^3} - \frac{c_\omega^2 k_n^3}{5\mu^2|_0 k_p^3}\left(2k_p^2\frac{\sqrt{k_n^2+m_*^2|_0}}{\sqrt{k_p^2+m_*^2|_0}} + \frac{c_\omega^2}{3\pi^2}\left[\frac{k_n^2 k_p^3}{\sqrt{k_n^2+m_*^2|_0}} + \frac{k_p^2 k_n^3}{\sqrt{k_p^2+m_*^2|_0}}\right]\right) \\
&\quad - \frac{c_\rho^2 k_n^3}{20\mu^2|_0 k_p^3}\left(2k_p^2\frac{\sqrt{k_n^2+m_*^2|_0}}{\sqrt{k_p^2+m_*^2|_0}} + \frac{c_\rho^2}{12\pi^2}\left[\frac{k_n^2 k_p^3}{\sqrt{k_n^2+m_*^2|_0}} + \frac{k_p^2 k_n^3}{\sqrt{k_p^2+m_*^2|_0}}\right]\right) \\
&\quad + \frac{c_\rho^2 c_\omega^2 k_n^3}{30\pi^2\mu^2|_0 k_p^3}\left[\frac{k_n^2 k_p^3}{\sqrt{k_n^2+m_*^2|_0}} - \frac{k_p^2 k_n^3}{\sqrt{k_p^2+m_*^2|_0}}\right] - \frac{3\pi^2}{5\mu^2|_0 k_p}\frac{k_n^2+m_*^2|_0}{\sqrt{k_p^2+m_*^2|_0}}.
\end{aligned}
\tag{A3}
$$

$$\mathcal{A}_0^0|_0 = -\frac{\pi^4}{k_p^2 k_n^2}\frac{\partial^2\Lambda}{\partial k_p \partial k_n}\bigg|_0 = c_\omega^2 - \frac{c_\rho^2}{4} + \frac{\pi^2}{k_p^2}\frac{m_*|_0\frac{\partial m_*}{\partial k_p}|_0}{\sqrt{k_n^2 + m_*^2|_0}}, \tag{A4}$$

$$\mathcal{B}_0^0|_0 = \frac{\pi^4}{k_n^5}\left(2\frac{\partial\Lambda}{\partial k_n}\bigg|_0 - k_n\frac{\partial^2\Lambda}{\partial k_n^2}\bigg|_0\right) = c_\omega^2 + \frac{c_\rho^2}{4} + \frac{\pi^2}{k_n^2}\frac{k_n + m_*|_0\frac{\partial m_*}{\partial k_n}|_0}{\sqrt{k_n^2 + m_*^2|_0}}, \tag{A5}$$

$$\mathcal{C}_0^0|_0 = \frac{\pi^4}{k_p^5}\left(2\frac{\partial\Lambda}{\partial k_p}\bigg|_0 - k_p\frac{\partial^2\Lambda}{\partial k_p^2}\bigg|_0\right) = c_\omega^2 + \frac{c_\rho^2}{4} + \frac{\pi^2}{k_p^2}\frac{k_p + m_*|_0\frac{\partial m_*}{\partial k_p}|_0}{\sqrt{k_p^2 + m_*^2|_0}} + \frac{\pi^2}{k_p}\frac{1}{\sqrt{k_p^2 + m_e^2}}. \tag{A6}$$

where

$$\frac{\partial m_*}{\partial k_n}\bigg|_0 = -\frac{c_\sigma^2}{\pi^2}\frac{m_*|_0 k_n^2}{\sqrt{k_n^2 + m_*^2|_0}}\left(\frac{3m - 2m_*|_0 + 3bmc_\sigma^2(m - m_*|_0)^2 + 3cc_\sigma^2(m - m_*|_0)^3}{m_*|_0}\right.$$
$$\left.-\frac{c_\sigma^2}{\pi^2}\left[\frac{k_n^3}{\sqrt{k_n^2 + m_*^2|_0}} + \frac{k_p^3}{\sqrt{k_p^2 + m_*^2|_0}}\right] + 2bmc_\sigma^2(m - m_*|_0) + 3cc_\sigma^2(m - m_*|_0)^2\right)^{-1}, \tag{A7}$$

$$\frac{\partial m_*}{\partial k_p}\bigg|_0 = -\frac{c_\sigma^2}{\pi^2}\frac{m_*|_0 k_p^2}{\sqrt{k_p^2 + m_*^2|_0}}\left(\frac{3m - 2m_*|_0 + 3bmc_\sigma^2(m - m_*|_0)^2 + 3cc_\sigma^2(m - m_*|_0)^3}{m_*|_0}\right.$$
$$\left.-\frac{c_\sigma^2}{\pi^2}\left[\frac{k_n^3}{\sqrt{k_n^2 + m_*^2|_0}} + \frac{k_p^3}{\sqrt{k_p^2 + m_*^2|_0}}\right] + 2bmc_\sigma^2(m - m_*|_0) + 3cc_\sigma^2(m - m_*|_0)^2\right)^{-1}. \tag{A8}$$

[1] C. O. Heinke and W. C. G. Ho, Astrophys. J. Lett. **719**, L167 (2010).

[2] D. Page, M. Prakash, J. M. Lattimer, and A. W. Steiner, Phys. Rev. Lett. **106**, 081101 (2011); P. S. Shternin, D. G. Yakovlev, C. O. Heinke, W. C. G. Ho, and D. J. Patnaude, Mon. Not. R. Astron. Soc. **412**, L108 (2011); D. Blaschke, H. Grigorian, D. N. Voskresensky, and F. Weber, Phys. Rev. C **85**, 022802 (2012); A. Sedrakian, Astron. Astrophys. **555**, L10 (2013).

[3] G. Baym, C. J. Pethick, D. Pines, and M. Ruderman, Nature (London) **224**, 872 (1969).

[4] P. W. Anderson and N. Itoh, Nature (London) **256**, 25 (1975).

[5] N. Andersson, K. Glampedakis, W. C. G. Ho, and C. M. Espinoza, Phys. Rev. Lett. **109**, 241103 (2012).

[6] N. Chamel, Phys. Rev. Lett. **110**, 011101 (2013).

[7] A. F. Andreev and E. P. Bashkin, Zh. Eksp. Teor. Fiz. **69**, 319 (1975) [Sov. Phys. JETP **42**, 164 (1976)].

[8] G. Comer and R. Joynt, Phys. Rev. D **68**, 023002 (2003).

[9] A. Kheto and D. Bandyopadhyay, Phys. Rev. D **89**, 023007 (2014).

[10] R. Prix, G. L. Comer, and N. Andersson, Astron. Astrophys. **381**, 178 (2002).

[11] R. Prix, J. Novak, and G. L. Comer, Phys. Rev. D **71**, 043005 (2005).

[12] M. Borumand, R. Joynt, and W. Klúzniak, Phys. Rev. C **54**, 2745 (1996).

[13] N. Chamel and P. Haensel, Phys. Rev. C **73**, 045802 (2006).

[14] M. E. Gusakov and P. Haensel, Nucl. Phys. **A761**, 333 (2005).

[15] M. E. Gusakov, E. M. Kantor, and P. Haensel, Phys. Rev. C **79**, 055806 (2009).

[16] G. Comer, Phys. Rev. D **69**, 123009 (2004).

[17] N. Andersson and G. L. Comer, Classical Quantum Gravity **18**, 969 (2001).

[18] G. L. Comer, Found. Phys. **32**, 1903 (2002).

[19] B. Carter, in *Relativistic Fluid Dynamics*, edited by A. Anile and M. Choquet-Bruhat (Springer, Heidelberg, 1989).

[20] G. L. Comer and D. Langlois, Classical Quantum Gravity **11**, 709 (1994).

[21] B. Carter and D. Langlois, Phys. Rev. D **51**, 5855 (1995).

[22] B. Carter and D. Langlois, Nucl. Phys. **B531**, 478 (1998).

[23] D. Langlois, A. Sedrakian, and B. Carter, Mon. Not. R. Astron. Soc. **297**, 1189 (1998).

[24] G. Comer, D. Langlois, and L. M. Lin, Phys. Rev. D **60**, 104025 (1999).

[25] R. Prix and M. Rieutord, Astron. Astrophys. **393**, 949 (2002).

[26] J. Boguta and A. R. Bodmer, Nucl. Phys. **A292**, 413 (1977).

[27] N. K. Glendenning, *Compact Stars* (Springer-Verlag, New York, 1997).

[28] J. B. Hartle, Astrophys. J. **150**, 1005 (1967).

[29] F. J. Fattoyev, C. J. Horowitz, J. Piekarewicz, and G. Shen, Phys. Rev. C **82**, 055803 (2010).

[30] J. B. Hartle and K. S. Thorne, Astrophys. J. **153**, 807 (1968).

[31] J. W. Hessels *et al.*, Science **311**, 1901 (2006).